Two-photon microendoscope for label-free imaging in stereotactic neurosurgery

TARAH A. WELTON,[1] NICHOLAS M. GEORGE,[2] BARIS N. OZBAY,[3] ARIANNA GENTILE POLESE,[4] GREGORY OSBORNE,[4] GREGORY L. FUTIA,[1] (iD) J. KEENAN KUSHNER,[2,5] BETTE KLEINSCHMIDT-DEMASTERS,[6,7,8] ALLYSON L. ALEXANDER,[8,9] AVIVA ABOSCH,[10] STEVEN OJEMANN,[8] DIEGO RESTREPO,[4] AND EMILY A. GIBSON[1,*]

[1]*Department of Bioengineering, University of Colorado Anschutz Medical Campus, Aurora, CO 80045, USA*
[2]*Neuroscience Graduate Program, University of Colorado Anschutz Medical Campus, Aurora, CO 80045, USA*
[3]*Intelligent Imaging Innovations, Denver, Colorado, 80216, USA*
[4]*Department of Cell and Developmental Biology, University of Colorado Anschutz Medical Campus, Aurora, CO 80045, USA*
[5]*Department of Pharmaceutical Sciences, Skaggs School of Pharmacy and Pharmaceutical Sciences, University of Colorado Anschutz Medical Campus, Aurora, CO 80045, USA*
[6]*Department of Pathology, University of Colorado School of Medicine, Aurora, CO 80045, USA*
[7]*Department of Neurology, University of Colorado School of Medicine, Aurora, CO 80045, USA*
[8]*Department of Neurosurgery, University of Colorado School of Medicine, Aurora, CO 80045, USA*
[9]*Division of Pediatric Neurosurgery, Children's Hospital Colorado, Aurora CO 80045, USA*
[10]*Department of Neurosurgery, University of Nebraska Medical Center, Omaha, NE 68198, USA*
[*]*EMILY.GIBSON@CUANSCHUTZ.EDU*

Abstract: We demonstrate a gradient refractive index (GRIN) microendoscope with an outer diameter of ~1.2 mm and a length of ~186 mm that can fit into a stereotactic surgical cannula. Two photon imaging at an excitation wavelength of 900 nm showed a field of view of ~180 microns and a lateral and axial resolution of 0.86 microns and 9.6 microns respectively. The microendoscope was tested by imaging autofluorescence and second harmonic generation (SHG) in label-free human brain tissue. Furthermore, preliminary image analysis indicates that image classification models can predict if an image is from the subthalamic nucleus or the surrounding tissue using conventional, bench-top two-photon autofluorescence.

1. Introduction

Parkinson's disease (PD) is one of the most prevalent neurodegenerative disorders in the world and affects approximately 572 out of 100,000 people who are over the age of 45 in North America [1]. As the disease progresses, patients experience a variety of motor and nonmotor symptoms which significantly impact their quality of life such as resting tremor, rigidity, bradykinesia (slowness of movement), akinesia (loss of voluntary movement), postural deformities and instability, autonomic dysfunction, sleep disorders, and cognitive, neurobehavioral, and sensory abnormalities [2]. Although the first line of treatment for PD remains dopaminergic medications, deep brain stimulation (DBS) surgery is now considered standard-of-care treatment for PD when medications no longer provide durable control of motor symptoms. DBS surgery involves the placement of chronically implanted electrodes, connected to a programmable generator, to deliver electrical stimulation to deep brain regions including the subthalamic nucleus (STN) or the internal part of the globus pallidus to treat the motor symptoms of PD [3]. The STN is the most

common target for electrode implantation when treating PD [4]. Accurate placement of the electrodes in the intended deep brain targets is critical to the therapeutic success of DBS surgery.

While there is a great deal of variation in how DBS surgeries are performed globally, neurosurgeons largely rely on a combination of stereotactic targeting, preoperative imaging, and microelectrode recordings and/or macrostimulation to locate deep brain targets for DBS [4]. Precisely targeting the STN is particularly challenging due to its location in the midbrain (roughly 9 cm from the cortical surface), its small size (20-30 mm^3), and a high degree of patient-to-patient variability in STN position relative to established anatomical landmarks and atlases [5]. Further challenges arise in the operating room where opening the skull and dura in a semi-sitting patient can shift the position of the brain relative to preoperative imaging (on which target planning has been performed) due to the outflow of cerebrospinal fluid and the influx of air [6].

Intraoperatively, neurosurgeons use microelectrode recordings (MER) to perform real-time electrophysiology along the surgical trajectory. This technique aids in target verification because different regions of the brain generate distinct neuronal activity patterns which can be used to pinpoint the current location of the microelectrode [7]. However, the accurate interpretation of MER requires specialized training and experience. The use of MER also increases the cost and duration of the DBS procedure and increases the risk of intracranial hemorrhage [7]. Furthermore, MER requires the patient to be awake and participating throughout the entire surgical procedure which can be both uncomfortable and anxiety provoking for the patient. Despite widespread use of MER in North America, a registry-based study found that the rate of DBS electrode revision or removal was between 15.2% and 34% [8]. The authors estimate that "up to 48.5% of revisions may have been due to improper targeting or a lack of therapeutic effect" [8]. Therefore, there is a clinical need to reduce or eliminate the use of MER in DBS surgery without compromising the accuracy of electrode positioning.

In recent years, numerous studies have been published regarding image-based target verification in the operating room. Reliance solely on image-based targeting – for DBS targets that are visible – would eliminate the need for MER and allow for patients to be placed under general anesthesia for the duration of the DBS surgery. These studies focused on the use of magnetic resonance imaging (MRI) or computed tomography (CT) to optimize electrode placement in the operating room with results that are comparable to MER based procedures [9–12]. MRI and CT are noninvasive and widely available in hospital settings, but they have a limited resolution and do not allow for real-time imaging during the procedure. Conversely, optical imaging methods provide high resolution and real-time imaging, but they require direct access to tissue and commonly employ exogenous dyes such as protoporphyrin IX (PpIX) or indocyanine green (ICG) to generate contrast [13]. Optical imaging methods like single-photon microscopy, multi-photon microscopy, and optical coherence tomography have been investigated for numerous applications in the operating room including imaging tumor margins, quickly assessing the viability of a biopsy samples, and detecting blood vessels [13–15].

Two-photon microscopy is particularly useful for imaging endogenous fluorescence, or autofluorescence, in biological samples. Autofluorescence originates from naturally occurring fluorophores such as reduced nicotinamide adenine dinucleotide (NADH), oxidized flavin adenine dinucleotide (FAD), and lipofuscin [16,17]. In addition to imaging autofluorescence, two-photon microscopy can simultaneously generate and image second harmonic generation (SHG) signals in tissues that contain fibrillar collagen like blood vessels [14,16]. The advantages of using two-photon microscopy as a supplement or replacement for MER include: reduced tissue damage by penetrating the tissue with light instead of sharp microelectrodes and high-resolution, real-time imaging along the surgical trajectory. Furthermore, the ability to visualize blood vessels in real-time may help to reduce the risk of intracranial hemorrhage during the procedure. Two-photon microscopy uses near-infrared wavelengths of light which results in intrinsic optical sectioning, reduced photobleaching, and deeper tissue penetration due to reduced scattering [16].

Since DBS surgery is performed through a narrow cannula with an inner diameter of ~1.1 mm, accessing and imaging deep brain regions in humans using two-photon microscopy presents a significant engineering challenge. Gradient refractive index (GRIN) lenses are rod shaped and have an index of refraction that varies as a function of the radius. While these types of lenses are predisposed to optical aberrations, they are also ideal for the fabrication of rigid microendoscopes due to their small outer diameters, long lengths, relatively high numerical apertures, and low cost [18]. GRIN lenses are commonly used for *in-vivo*, deep brain imaging in rodents because they allow researchers to physically bypass the scattering tissue overlaying a region of interest [19–21]. Previous studies have demonstrated that GRIN lenses are also capable of imaging fluorescence and SHG in unlabeled tissues [22–26]. While GRIN lenses are used quite extensively in research, their application in clinical settings has thus far been limited [24–28].

Here, we use conventional, benchtop two-photon microscopy to assess if the human STN can be distinguished from the surrounding tissue using endogenous tissue signals and perform a preliminary spectral evaluation of the resulting autofluorescence. We also test four rudimentary image classifiers to see if they are able to reliably determine if an image came from the STN or the surrounding tissue. Finally, we design and characterize a prototype GRIN microendoscope that is 186 mm long and 1.2 mm in outer diameter. Proof of concept tissue imaging is performed to demonstrate that our novel microendoscope is capable of imaging autofluorescence and SHG in label-free, *ex-vivo* mouse and human brain tissue.

2. Materials and methods

2.1. Post-mortem human brain tissue dissection and label-free imaging

We obtained postmortem human brain tissue from the Department of Pathology at the University of Colorado Anschutz Medical Campus. The tissue was briefly stored in formalin before being immersion fixed with freshly made 4% paraformaldehyde. We performed a gross dissection to isolate a region of the midbrain containing the globus pallidus, substantia nigra, and STN. The isolated samples were cryopreserved in 30% sucrose, frozen in OCT, and sectioned on a cryostat at 40 microns thick. Tissue sections were mounted on slides using VECTASHIELD Plus mounting medium (H-1900, Vector Laboratories) for imaging (Fig. 1). Because we were interested in utilizing label free imaging techniques to visualize this region of the brain, no exogenous labels or stains were applied to the samples.

2.2. Resected human tissue sample preparation

Prior to the initiation of this study, approval was obtained through the Colorado Multiple Institutional Review Board (COMIRB Protocol 09-0906). A 20-year-old male patient underwent temporal lobectomy for intractable epilepsy after a full pre-surgical evaluation was completed, including stereotactic electroencephalogram (EEG) to localize the seizure focus. The patient provided written, informed consent for the use of his tissue and de-identified information. The surgery was performed at Children's Hospital Colorado at Anschutz Medical Campus in Aurora, Colorado. Histopathological evaluation revealed gliosis.

Immediately following the surgical resection, resected neocortical tissue was submerged in 0-4°C carbogenated (95%O2-5% CO2) N-methyl-D-glucamine (NMDG) substituted artificial cerebrospinal fluid (ACSF), adapted from Ting et al.: ((in mM) 92 NMDG, 2.5 KCl, 1.25 NaH2PO4, 30 NaHCO3, 20 4-(2-hydroxyethyl)-1-pip-erazineethanesulfonic acid (HEPES), 25 d-glucose, 2 thiourea, 5 Na-ascorbate, 3 Na-pyruvate, 0.5 CaCl2·4H2O and 10 MgSO4·7H2O, pH adjusted to 7.3-7.4 with concentrated hydrochloric acid (HCl), osmolality~ 305mOsm/kg) [29]. The tissue was transported to the laboratory in ice-cold saline, approximately 15-20 minutes in transit time. The tissue was then placed in a petri dish with 0-4°C carbogenated NMDG ACSF. Approximately 1 cm^3 tissue blocks were sectioned. No effort was made to remove the connective
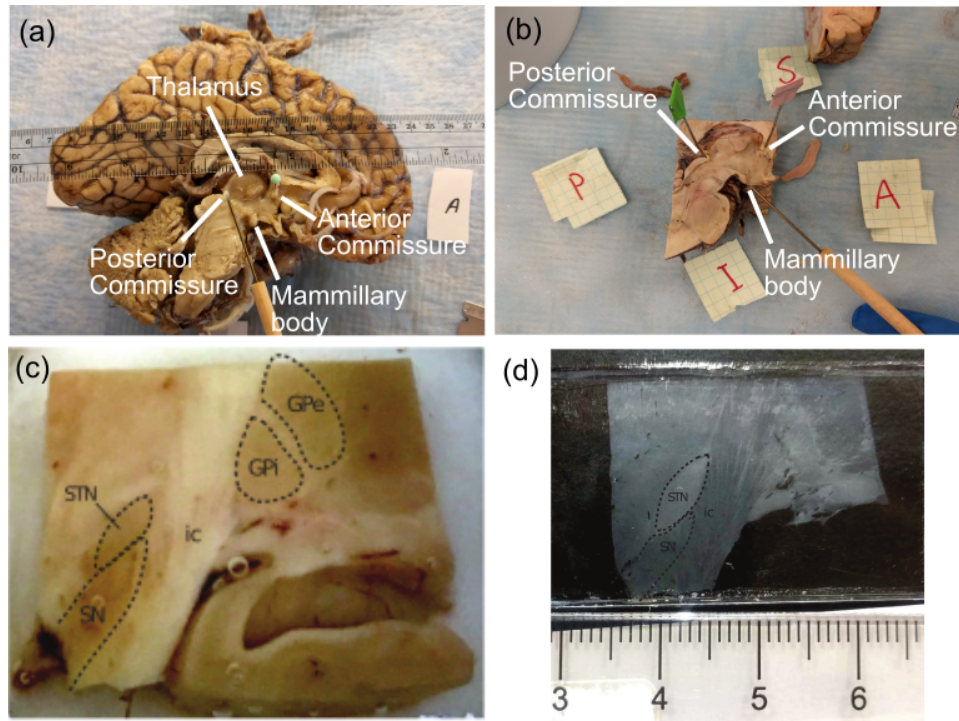
Fig. 1. Gross dissection and slide mounting of human brain tissue samples. (a) Human brain cut in the sagittal plane at the midline. Important landmarks are labeled in the image. (b) Isolated midbrain region with important landmarks labeled. The paper cutouts mark the anatomical directions: posterior (P), superior/dorsal (S), anterior (A), and inferior/ventral (I). (c) Example section of the midbrain with regions of the basal ganglia delimited. Subthalamic nucleus (STN), substantia nigra (SN), internal capsule (ic), internal globus pallidus (Gpi), and external globus pallidus (GPe). (d) A 40-micron thick cryostat sectioned sample from (c) mounted for imaging. Regions of interest are labeled as indicated in (c).

tissue, blood vessels, or the pia mater. The unfixed human brain tissue was then transferred to a 6-well cell culture plate on ice containing enough cold 0.9% saline solution (diluted in ddH20) to submerge the tissue block.

During imaging, the sample was transferred to a 35×10 mm petri dish (153066, ThermoFisher Scientific), placed on the sample stage, and raised until the tissue surface was flush with the GRIN microendoscope. 0.9% saline solution was added to the dish until the tissue was submerged. All imaging was completed within ~5.5 hours of the surgery.

2.3. GRIN microendoscope design and fabrication

The initial design of the GRIN microendoscope was completed using optical design software (OpticStudio, ZEMAX). The system was optimized to achieve a desired length of ~ 180 mm and an imaging numerical aperture (NA) > 0.45. The final design is a combination of four GRIN lenses (two stock and two custom) separated by small air spaces (Fig. 2(a)). This configuration results in near-diffraction limited imaging with a Strehl ratio of ~ 0.873 on axis and a theoretical imaging NA of 0.384 which is slightly lower than the 0.45 target. The Seidel diagram indicates that spherical aberration is the largest aberration present in the design (See Supplement 1, Fig. S1. for ZEMAX simulation results).
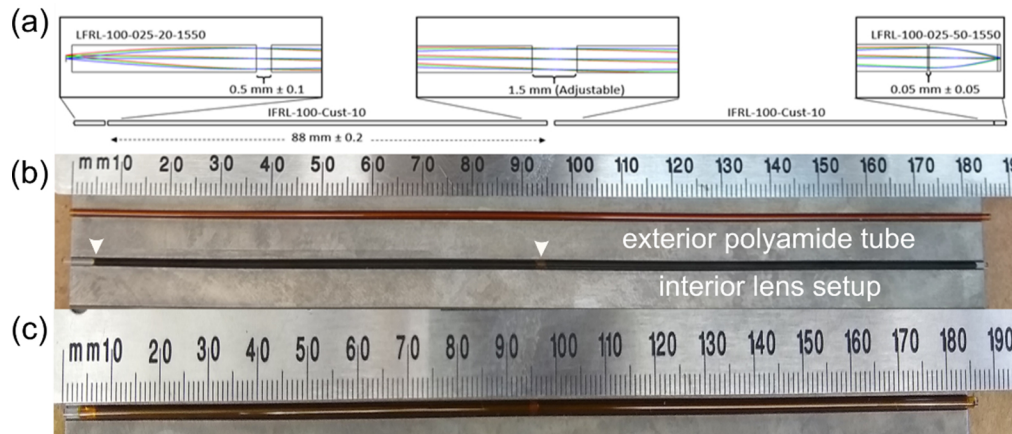
Fig. 2. Fabrication of the GRIN microendoscope prototype. (a) ZEMAX schematic of the GRIN microendoscope, (b) Image of the interior lenses and spacers which are denoted by the white arrows, and (c) Image of the completed prototype which is ~186 mm long and 1.2 mm in OD.

A prototype of the GRIN microendoscope was fabricated using lenses from GRINTECH GmbH (Table 1). The small interior air spaces in the design were maintained by annular, polyamide spacers manufactured and trimmed by MicroLumen Inc (Fig. 2(b)). The spacers had custom lengths of 0.5 mm ± 0.13 mm and 1.5 mm ± 0.13 mm and a wall thickness of ~0.05207 mm ± 0.0006 mm (inner diameter (ID): 0.94996 mm, outer diameter (OD): 1.0541 mm). The prototype exterior was also composed of polyamide tubing with an ID of 1.06 mm and an OD of 1.21 mm (Code 420-III, MicroLumen Inc.).

Table 1. Lens properties and manufacturing tolerances

Product Code	Quantity	Diameter (mm)	Length (mm)	Pitch	Numerical Aperture (NA)
LFRL-100-025-20-1550	1		$6.16 \pm 5\%$	0.25	0.2
IFRL-100-Cust-10	2	$1.0 + 0/ - 0.01$	$88 \pm 5\%$	~0.98	0.1
LFRL-100-025-50-1550	1		$2.29 \pm 5\%$	0.25	0.5

The GRIN microendoscope was assembled by partially inserting the 0.5 NA GRIN lens into the end of exterior tubing, and an insect pin was used to apply superglue (Ultra Gel Mini, Locite) around the joint where the tubing and lens met. Additional lenses and spacers were added sequentially. The polyamide tube was trimmed so that the 0.2 NA GRIN lens would protrude slightly and the joint between the lens and the exterior sheath was sealed with superglue. The completed GRIN microendoscope prototype is approximately 186 mm long and 1.2 mm in outer diameter (Fig. 2(c)).

2.4. GRIN microendoscope experimental setup

2.4.1. Two-photon microscope setup

The optical performance of the microendoscope was tested on a custom built two-photon microscope (Fig. 3). The microscope used a Ti:Sapphire laser with a built-in dispersion compensation DeepSee module (Mai Tai HP DS, Spectra Physics), and imaging was performed at an excitation wavelength of 900 nm. The laser power was controlled using a halfwave plate and Glan Thompson Polarizer. A variable beam expander (87-546, Edmund Optics) was used to

adjust the size of the beam at the back aperture of the objective. The beam path could be optionally diverted into a custom-built pulse compressor using two mirrors attached to a translation stage. A quarter wave plate was used to circularly polarize the light through the compressor to improve the efficiency of the diffraction polarization gratings (16-592, Edmund Optics). SHG excitation of collagen fibers and, consequently, blood vessels, is dependent on the orientation of the fibers relative to the polarization of the excitation laser (e.g. parallel or perpendicular). Circularly polarizing the laser beam through the pulse compressor allowed us to excite all of the collagen fibers in the field of view independent of their orientation [30].
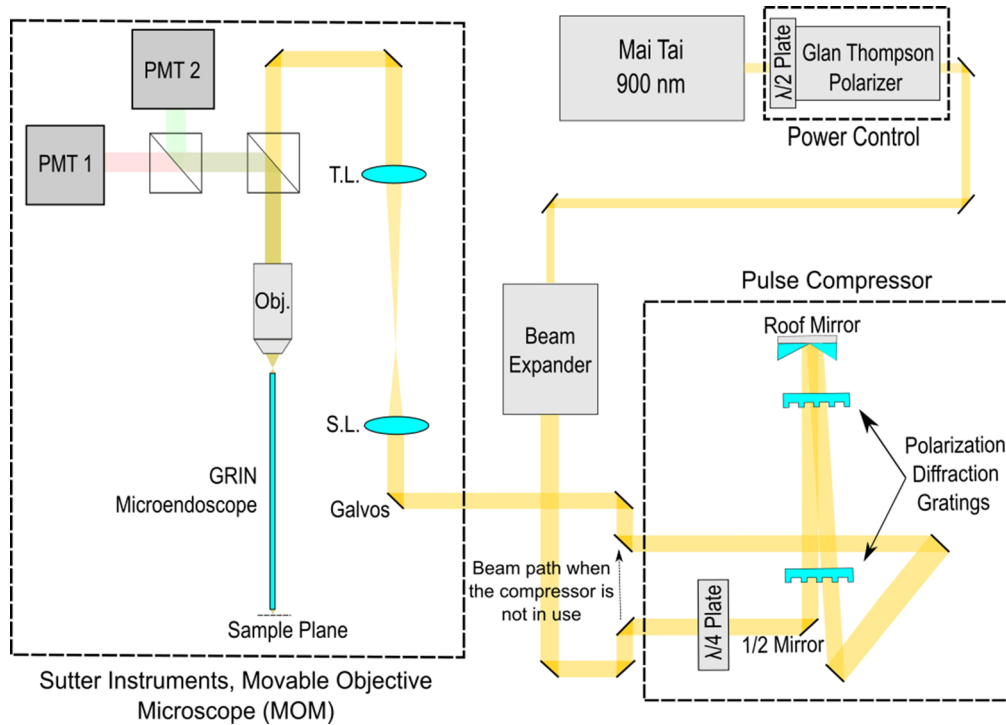

Fig. 3. Schematic of the custom-built, two-photon microscope using an upright Sutter Movable Objective Microscope (MOM). The microscope is equipped with a scan lens (S.L.) (f ~ 35 mm), tube lens (T.L.) (f = 200 mm), and two filter sets for the PMTs. Images of green fluorescence (calibration target, fluorescent beads, and EGFP labeled tissue) were captured using filters for 525 ± 35 nm (PMT 2). Images of autofluorescence and SHG were captured using filters for 540 ± 25 nm (PMT 1) and 450 ± 5 nm (PMT 2) respectively. An Olympus 10x, 0.4 NA objective (Obj.) was used to couple light into the GRIN microendoscope. The image collected by the GRIN microendoscope is acquired by raster scanning in xy with the microscope's galvanometric scanning mirrors (Galvos), and the focal plane (z) is adjusted by moving the position of the 10x objective relative to the top of the GRIN microendoscope.

All microendoscope experiments were performed on a Movable Objective Microscope (Sutter Instruments) with galvanometric scanning. An air objective (Olympus UplanSApo 10x, 0.4 NA) was used to couple light into the GRIN microendoscope. The microendoscope was secured in a cage system using custom 3D printed disks and Buna-N-Nitrile O-rings (B900002, The O-Ring Store LLC) which created a press fit between the cage and the GRIN microendoscope (Fig. 5(b)). Two manual goniometers were used to adjust the pitch and roll of the microendoscope relative to the objective and the sample stage, and a manual translation stage allowed for course adjustments in the vertical direction. A motorized micromanipulator (MP-225, Sutter Instruments) equipped

with a right-angle adapter was used as a sample stage to allow for precise control of the distance between the imaging end of the GRIN microendoscope and the sample (Fig. 5(a)).

Fluorescence from the sample plane was spectrally separated using a dichroic mirror and bandpass filters. The fluorescent signal was detected using two Photomultiplier Tubes (PMTs) (H11706P-40, Hamamatsu). Two different filter sets were used for imaging: 1) images of a green, florescent calibration target (DA113, II-VI Aerospace & Defense) (Fig. 8), green, fluorescent beads suspended in agarose (Fig. 9), and enhanced green florescent protein (EGFP) labeled oligodendrocytes (Fig. 10(a)) were captured using PMT2 with a filter for 525 ± 35 nm (ET525/70 M-2P, Chroma), and 2) images of autofluorescence and SHG (Fig. 10(b)-10(d)) were captured simultaneously using PMT 1 and PMT 2 with filters for 540 ± 25 nm (HQ540/50, Chroma) and 450 ± 5 nm (7388, Alluxa) respectively. The autofluorescence/SHG filters were separated by a dichroic mirror that transmitted light > 500 nm to PMT1 as determined by a spectrophotometer. Images were collected using Slidebook imaging software (Intelligent Imaging Innovations) and analyzed using Fiji [31], Excel (Microsoft), and MATLAB (R2018a, MathWorks).

2.4.2. Pulse compressor for dispersion compensation through GRIN microendoscope

The two-photon fluorescent signal is inversely proportional to the pulse duration. The DeepSee module on the Mai Tai allowed for dispersion correction with a maximum group delay dispersion (GDD) of ~ 15700 fs^2. This was sufficient to collect images of EGFP labeled oligodendrocytes through the GRIN microendoscope using an average power of ~ 20 mW in the sample plane. However, the system was incapable of clearly resolving autofluorescence in fixed, mouse brain tissue at average powers up to 30 mW. Figure 4(a) shows the mean fluorescent signal collected through the GRIN microendoscope as a function of the GDD of the DeepSee module. The signal plateaued at the negative end of the DeepSee module's tuning range without a clear maximum, indicating that we did not achieve the shortest pulse (Fig. 4(a)). These measurements suggested that dispersion compensation from the DeepSee module alone was not sufficient to correct for the combined dispersion of the microscope system and the GRIN microendoscope.

Therefore, we constructed a double-pass pulse compressor in a Treacy configuration using diffraction polarization gratings (16-592, Edmund Optics) with 190 grooves/mm. These gratings selectively diffract circularly polarized light into the positive or negative first order with high efficiency. Average power measurements taken at the back aperture of the microscope objective show that the transmission efficiency of the compressor was approximately 42%. The distance between the grating pairs was optimized experimentally by incrementally adjusting the separation of the gratings using an optical rail and cycling through the DeepSee module's tuning range during imaging. The objective of this procedure was to find a combination of parameters between the pulse compressor and the DeepSee module that would maximize the mean fluorescent signal in the sample plane of the GRIN microendoscope. A maximum was achieved when the gratings were positioned 19.5 cm apart, and the GDD of the DeepSee module was set to $\sim$ -12800 fs^2 (Fig. 4(a)). Theoretically, a grating distance of 19.5 cm and an incident angle of 0° results in a GDD of $\sim$ -19000 fs^2 from the pulse compressor (Fig. 4(b)). Between the Treacy pulse compressor and the DeepSee module, the total second order compensation of the system was roughly -31,800 fs^2.

The performance of the pulse compressor was verified using frequency resolved optical gating (FROG) (FROGscan Ultra, MesaPhotonics). A 40X, 0.5 NA reflective objective (LMM-40X-PO1, THORLabs), a right-angled mirror, and two steering mirrors were used to direct the beam exiting the GRIN microendoscope into the FROG where it was focused onto a SHG crystal. VideoFROGscan software (Version 9.5, MesaPhotonics) was used to reconstruct the pulse temporal intensity and phase. This confirmed that the pulse compressor restored the pulse width to < 100 fs in the sample plane of the GRIN microendoscope (Fig. 4(c) & 4(d)).
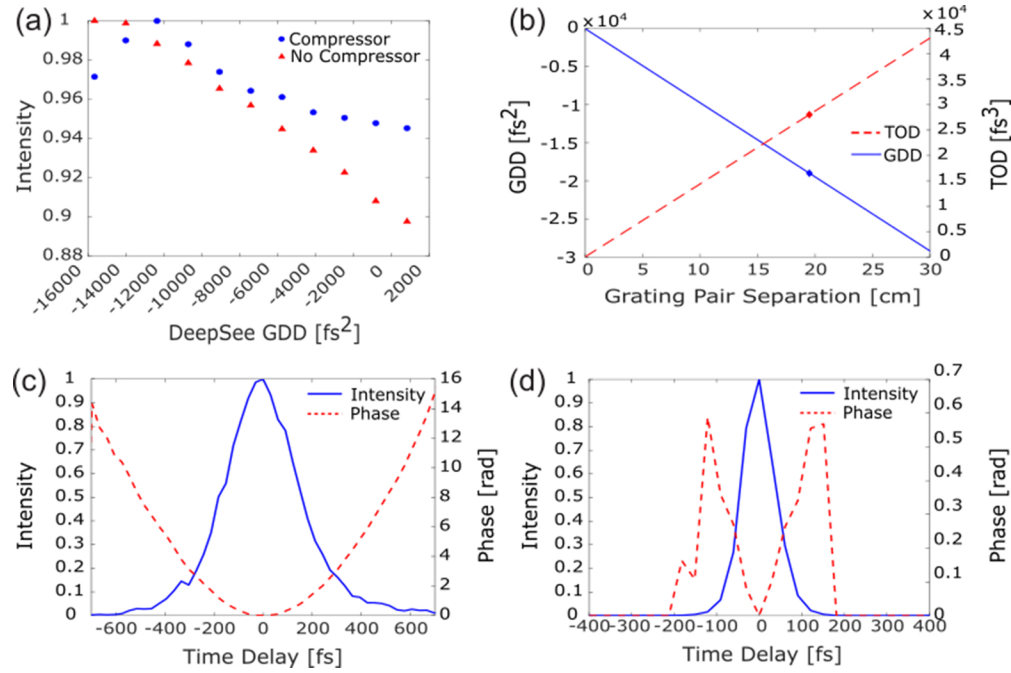
Fig. 4. Dispersion Modeling and Pulse Compression. (a) Mean fluorescent signal through the GRIN microendoscope over the DeepSee tuning range with (blue, circles) and without (red, triangles) the Treacy compressor engaged. The diffraction gratings were separated by 19.5 cm, (b) Mathematical modeling of second order (GDD) (blue, solid line) and third order dispersion (TOD) (red, dotted line) as a function of the distance between two diffraction gratings. The blue and red diamonds represent the theoretical GDD ($\sim$-19000 fs^2) and TOD ($\sim$28100 fs^3) values at a grating distance of 19.5 cm, (c) Frequency Resolved Optical Gating (FROG) reconstruction of the pulse intensity (solid, blue line) and phase (red, dotted line) in the sample plane of the GRIN microendoscope when the compressor is NOT in the beam path and the DeepSee GDD is $\sim$-15700 fs^2. The retrieved pulse width is $\sim$335 fs, and (d) FROG reconstructed pulse intensity (blue, solid line) and phase (red, dotted line) in the sample plane of the GRIN microendoscope when the compressor is in the beam path and the DeepSee GDD is $\sim$ -12800 fs^2. The retrieved pulse width is $\sim$91 fs.

2.4.3. GRIN microendoscope alignment

The microscope alignment was tested prior to each imaging session. The GRIN microendoscope was secured to the floating table using a custom cage system (Fig. 5(a)), and a level was used to manually orient the sample stage. Both ends of the microendoscope were cleaned using lens tissue and 100% methanol or ethanol, and it was threaded through two 3D printed disks equipped with Buna-N Nitrile O-Rings (B900002, The O-Ring Store, LLC) (Fig. 5(b)). A green, fluorescent flat was used to roughly align the Olympus 10x objective with the microendoscope using widefield illumination. The microscope's widefield camera was employed to verify that the optical axis of the 10x objective and the microendoscope were aligned by adjusting the pitch/roll goniometers so that the top surface of the microendoscope came into focus at roughly the same time [19]. Finally, a fluorescent calibration target (DA113, II-VI Aerospace & Defense) was imaged using two-photon microscopy to finetune the position of the objective relative to the microendoscope by centering the resulting image in the image acquisition software (see Fig. 8 for an example of a maximum intensity projection of a centered fluorescent grid).
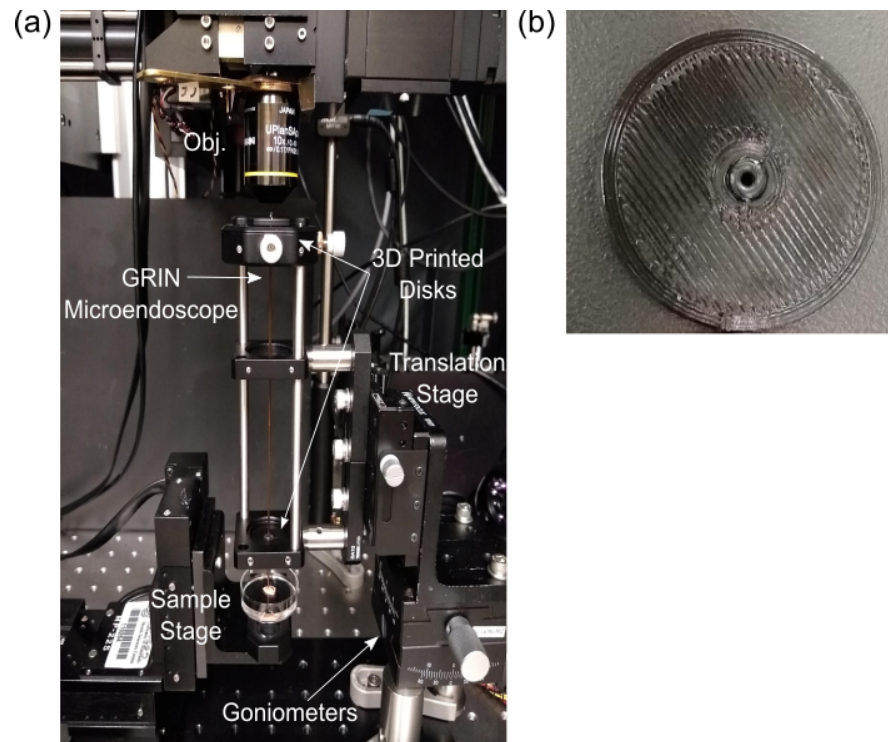
Fig. 5. GRIN microendoscope experimental setup. (a) Image of a custom-built cage system used to hold the GRIN microendoscope. The GRIN microendoscope is secured in a press-fit by two 3D printed disks with flexible O-rings. A manual translation stage and two goniometers were used to adjust the vertical position and the pitch/roll of the GRIN microendoscope relative to the objective (Obj.) and the sample stage during alignment. The sample stage is a motorized micromanipulator with a right-angle adapter which allowed for precise adjustment of the sample position relative to the GRIN microendoscope. The sample shown in the image is unfixed, human temporal lobe suspended in a saline solution. (b) Close-up image of a 3D printed disk with attached O-ring.

2.4.4. GRIN microendoscope sample working distance

When imaging flat samples, like the calibration target, the sample was placed on the sample stage and raised until it was flush with the bottom of the GRIN microendoscope (i.e., a gentle nudge would not dislodge the slide). The stage position was noted, and the working distance (WD) was calculated relative to this position. For example, a sample WD of 50 microns corresponds to a sample position that is 50 microns lower than when the slide was flush with the microendoscope.

2.4.5. Power measurements

A power meter (PM100A, THORLabs) and thermal sensor (S470C, THORLabs) were used to take average power measurements without galvo scanning. Measurements in the sample plane of the GRIN microendoscope were taken after aligning the microendoscope per the procedure above.

2.4.6. Bead sample preparation

The lateral and axial resolution of the GRIN microendoscope was measured using fluorescent beads suspended in agarose gel. A 5 mL sample of 0.5% low melting point agarose (A9414,

Sigma-Aldrich) was prepared with Millipore water. As the agarose was cooling, 0.2-micron (F8811, ThermoFisher Scientific) and 2-micron (L4530, Sigma Aldrich) green, fluorescent beads were stirred into the mixture at concentrations of 3.0×10^7 beads/mL and 2.8×10^4 beads/mL respectively. The 2-micron beads were added to make the sample easier to visualize when imaging. The agarose-bead mixture was poured into a 35×10 mm petri dish (153066, ThermoFisher Scientific) and allowed to set at room temperature in a dark location. During imaging, the dish was placed on the sample stage and raised until the agarose enveloped the tip of the GRIN microendoscope. Samples were capped, wrapped in parafilm, and stored long term at 4°C.

2.4.7. Potato starch sample preparation

A small red potato was cut in half, and a razor blade was used to scrape some potato starch onto a microscope slide. The slide was placed on the sample stage and raised until the glass was flush with the GRIN microendoscope. The position of the sample stage was noted, and the slide was lowered and repositioned so that the microendoscope was over the potato starch. Water was added to the starch, and the slide was raised to a WD of ∼ 100 microns for imaging.

2.4.8. Mouse tissue sample preparation

All animal procedures were performed under approval from the Institutional Animal Care and Use Committee (IACUC) at the University of Anschutz Medical Campus under guidelines from the National Institutes of Health. Two types of mouse brain tissue were imaged with the GRIN microendoscope: 1) 300-micron thick coronal slices of transgenic, PLP-EGFP tissue where the oligodendrocytes are labeled with EGFP [32] and 2) 500-micron thick sagittal slices of C57BL/6 (Jackson Laboratory) tissue. Wildtype samples were post-fixed in 4% paraformaldehyde, cut into sagittal slices on a vibratome, and stored in 1X PBS with 0.02% sodium azide (NaN_3). During imaging, a tissue slice was placed on a microscope slide, and the sample stage was raised until the tissue was pressed flush with the microendoscope. 1X PBS was added to keep the tissue moist and create a liquid interface between the tissue and the microendoscope.

3. Results

3.1. *Proof of concept human tissue imaging*

3.1.1. Label-free imaging of fixed, *post-mortem* human brain tissue

The primary objective of this experiment was to determine if the STN and blood vessels were distinguishable from the surrounding tissue using label-free, multiphoton imaging techniques on a conventional benchtop microscope. Slices of fixed, unlabeled human brain tissue were imaged using two-photon microscopy. Imaging was performed on a Zeiss Laser Scanning Microscope (LSM) 780 equipped with a 32-channel spectral QUASAR detector and a tunable Coherent Chameleon Ultra II: Ti-Sapphire laser.

The STN was clearly delineated by a higher density of autofluorescence puncta as compared to neighboring regions over a range of excitation wavelengths (850 nm to 950 nm). Figure 6(a) depicts a portion of the STN and surrounding region at an excitation wavelength of 950 nm. SHG signal was detected from what are presumably collagen-rich capillaries throughout the sample (Fig. 6(a) & Fig. 6(b)). The QUASAR detector was used to quantitatively evaluate the emission spectra of the autofluorescence by measuring the mean fluorescent intensity of a region of interest (ROI) across a wide spectral range (415 nm to 691 nm using ∼9 nm bins) at excitation wavelengths of 850 nm and 900 nm. These measurements confirmed that the autofluorescence is spectrally broad (Fig. 6(c)). This initial test demonstrated that it was possible to identify the STN and blood vessels from endogenous signals in fixed human samples using two-photon microscopy.
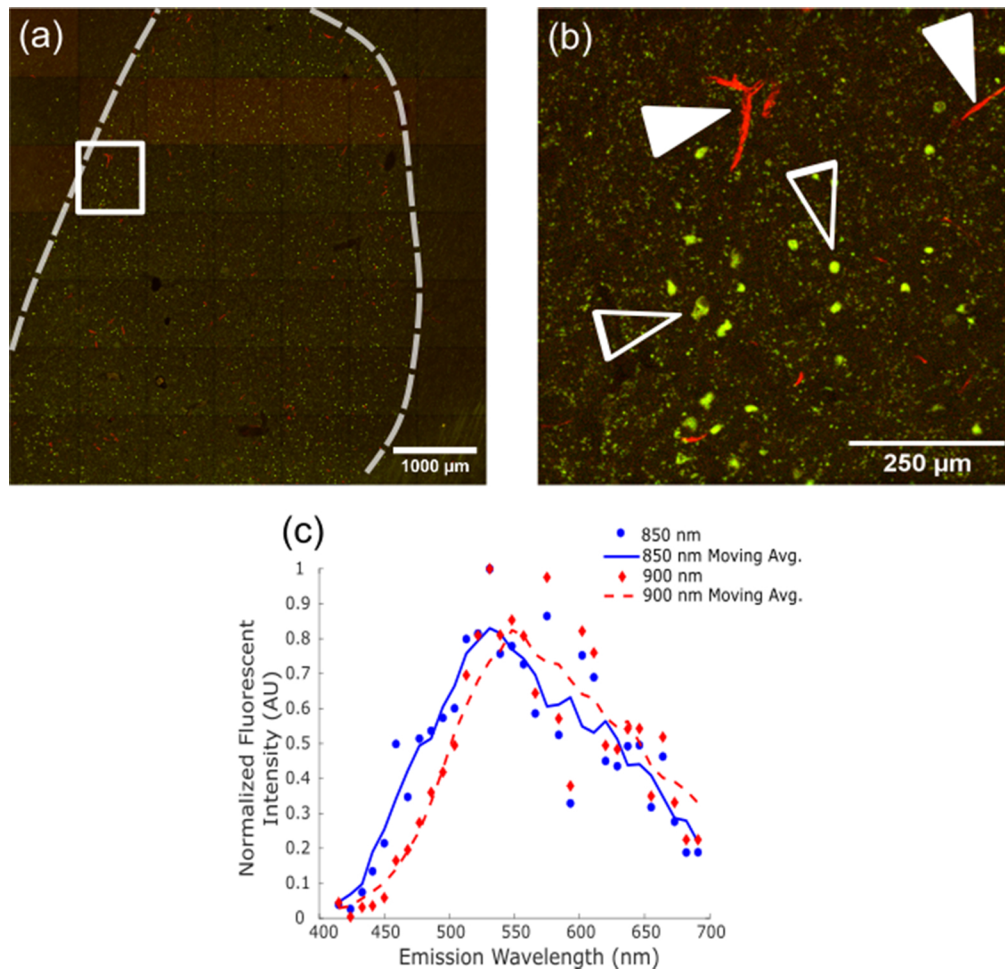
Fig. 6. Label-free imaging and autofluorescence characterization of human brain tissue. (a) Tiled image of the human STN at a two-photon excitation wavelength of 950 nm. Green represents autofluorescence, and red depicts SHG. The dashed lines represent the inferred boundaries of the STN based on gross anatomy and autofluorescence. (b) Solid box region enlarged from (a). SHG signal (red) is indicated by solid arrowheads and most likely arises from collagen-rich capillaries. Open arrowheads accentuate fluorescent puncta. (c) Normalized fluorescent emission spectra measured by the QUASAR detector. The circles and diamonds represent the mean fluorescent intensity over a ROI while the solid and dotted lines represent the moving average of the data. Two different excitation wavelengths were tested: 850 nm and 900 nm.

3.1.2. Using an image classifier to identify the STN

Because of the difference in the spatial distribution of autofluorescence between the STN and the surrounding brain regions (Fig. 6), we tested whether different image classifiers could reliably determine whether an image was taken in the STN or outside. To generate features for image classification, texture-based features were calculated using a grey level co-occurrence matrix (GLCM). The GLCM is a quantitative method for summarizing the occurrence of certain pixel values in pairs of pixels across an image and provides a quantitative measurement of the image

"texture" [33,34]. GLCM features have been widely used for medical image classification and analysis, especially in the fields of radiology and histology [35–38].

Z-stacks were collected with a 20X objective (Plan-Apochromat 20x/0.8 M27, Zeiss) using a two-photon microscope (Zeiss LSM 780) and an excitation wavelength of 950 nm. Maximum intensity images were created in Fiji and saved as tiff files for texture analysis. We used Cell Profiler 4.2.5 to calculate the GLCM features for a set of manually labeled images taken inside and outside of the STN [39]. For 2D images, Cell Profiler automatically calculates the Haralick GLCM features for four different directions or angles. We calculated the mean and range of each feature across the four angles to create rotation invariant features for classification [33]. GLCM features were calculated for two different grayscale levels (256 and 8) and five different scales (1, 3, 5, 10, and 20 pixels). Scale refers to the distance between the pixels that are used to calculate the GLCM features.

We used the features from this dataset to train four different classification models: linear discriminate analysis (LDA), support vector machine (SVM), naïve Bayes (NB), and a random forest (RF) classifier. The initial dataset consisted of 43 images from the two donors described in Table 2. Eight images were from donor H001, and 35 images were from donor H002. Of the 43 images, 23 were from inside of the STN and 20 were from outside of the STN.

Table 2. Machine learning dataset demographics

Donor	PD Diagnosis	Age	Hemisphere	Sex	Time in PFA
H001	No	52	Right	Male	2.5 weeks
H002	Yes	64	Right	Male	3 weeks

Bootstrapping was used to randomly select 43 images from the total dataset with resampling for 35 trials. The bootstrapped data was passed to our machine learning algorithms for training and testing. Leave one out (LOO) and three-fold cross validation were both used to assess the model's performance and prevent over-fitting. The random forest classifier performed the best on this dataset with a mean accuracy of 96% ± 3.0% (Fig. 7). Using Welch's t-test, we rejected the null hypothesis that the means of the un-shuffled and shuffled data were equal (all four p-values were < 0.001 and the false discovery rate was 0.05 [40]). The t-test is robust to non-normal distributions given enough data, but we verified the t-test results of any non-normal distribution using the Wilcoxon Rank Sum test which also rejected the null hypothesis that the medians of the un-shuffled and shuffled data were equal (p-value < 0.001) [41]. Normality was assessed using the Anderson-Darling test. Based on these preliminary results, we believe that future exploration of automated STN identification with larger, more diverse datasets is warranted and could provide an effective method for improving DBS probe placement.

3.2. Evaluating the optical performance of GRIN microendoscope

3.2.1. Magnification

The magnification of the GRIN microendoscope was determined experimentally by taking a 3D image of a green, fluorescent grid target through the microendoscope. A 256-micron z-stack was converted into a maximum intensity projection image, and six different measurements of image pitch were collected using the line feature in Fiji. Magnification was calculated as the ratio of the image pitch relative to the known pitch of the grid target (50 microns). The microendoscope's magnification at WDs of 0 microns and 250 microns is 2.9 ± 0.02 (n = 6) and 2.7 ± 0.03 (n = 6) respectively. In conjunction with the 10x Olympus objective, the total magnification of the imaging system is ~ 28x.
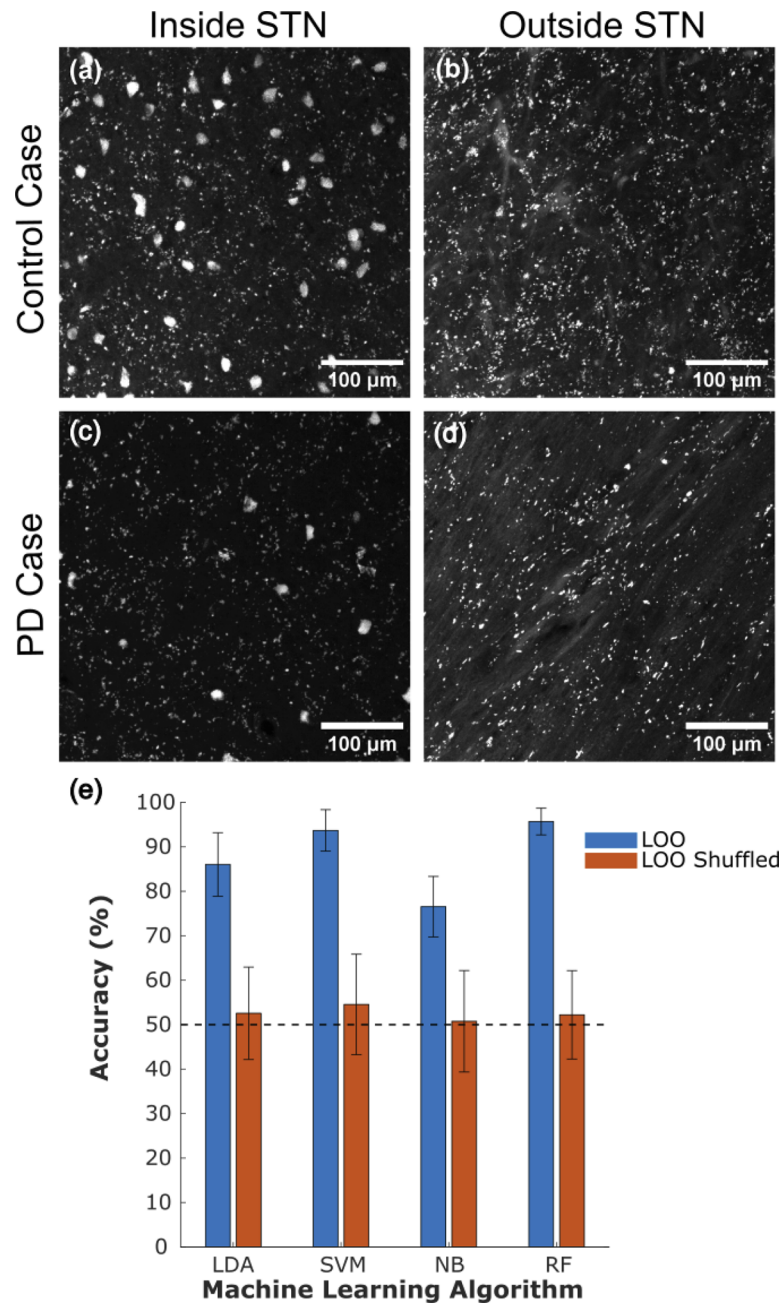
Fig. 7. Image classification performance across four different models with leave one out (LOO) validation, a GLCM scale of 5 pixels, and 256 grayscale levels. These parameters were selected because they resulted in the highest mean accuracy score. (a & c) Representative maximum intensity projection of autofluorescence inside of the STN for the control case (Donor H001) and the PD case (Donor H002) respectively, (b & d) Representative maximum intensity projection of autofluorescence from outside of the STN for the control case (Donor H001) and PD case (Donor H002) respectively, and (e) Bar graph showing the mean accuracy and standard deviation of each machine learning algorithm for the un-shuffled, bootstrapped data (blue) and the shuffled, bootstrapped data (orange).
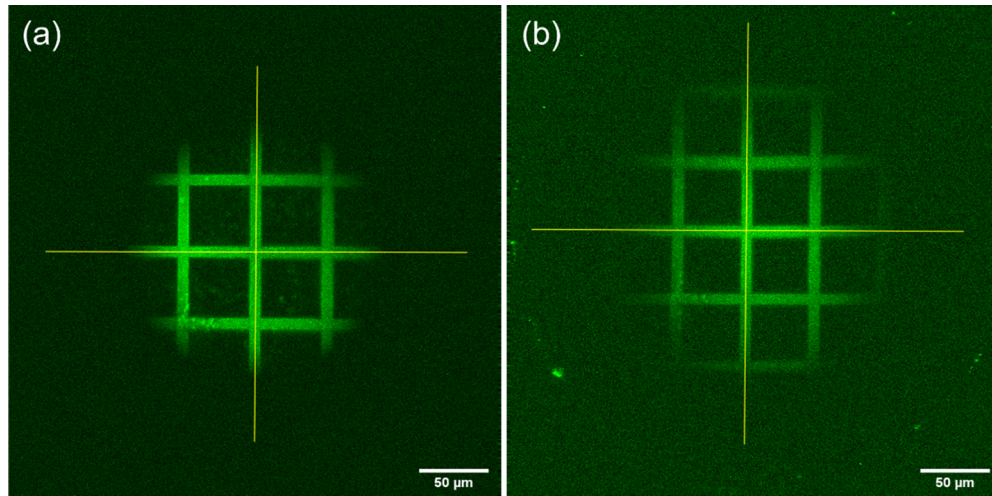
Fig. 8. Field of View (FOV) through the GRIN microendoscope at (a) a WD of 0 microns and (b) a WD of 250 microns. The scale bar is 50 microns.

3.2.2. Field of view

The field of view (FOV) of the GRIN microendoscope was calculated using a 3D image of the green, fluorescent grid target at different sample WDs. Any images where the PMT tripped during acquisition were discarded, and the remaining images in the 256-micron z-stack were converted to a maximum intensity projection using Fiji. Two lines were drawn across the FOV in the horizontal and vertical directions (Fig. 8(a) & 8(b)), the intensity profile was plotted, and the data was saved in an Excel worksheet for further analysis. MATLAB was used to normalize the intensity data, subtract the background, and apply a moving average to smooth out the profile. The FOV was calculated as the distance where the fluorescent intensity dropped to 10% of the maximum [19].

This calculation was performed on data collected during three different imaging sessions to determine if this measurement remained consistent when using our alignment procedure. The average FOV and standard deviation at each WD were calculated using three horizontal measurements and three vertical measurements. Table 3 summarizes the results which show that the FOV measurements differ slightly between the horizontal and vertical axis and there is substantial variability in the measured FOV between trials probably due to misalignments in the system even with the alignment procedure in place. Overall, the size of the FOV and the variability associated with the measurement increase as the distance between the microendoscope and the grid target increases.

Table 3. Average FOV through the GRIN Microendoscope at different sample WDs (n = 3)

Working Distance (microns)	Average Horizontal FOV ± SD (microns)	Average Vertical FOV ± SD (microns)
0	174 ± 1.89	180 ± 2.88
50	174 ± 6.69	175 ± 3.71
100	169 ± 7.01	178 ± 4.14
150	167 ± 9.24	185 ± 2.96
200	174 ± 6.89	189 ± 9.46
250	170 ± 7.60	199 ± 10.0

3.2.3.   Resolution

The resolution of the system was characterized by imaging 0.2-micron and 2-micron fluorescent beads suspended in agarose gel. Five beads across the FOV were randomly selected for analysis (Fig. 9(a)). Z-stacks of the beads were collected by moving the microscope objective vertically relative to the top surface of the microendoscope which remained stationary. Because the GRIN microendoscope acted as a relay for objective's focus, the z step size in the sample plane was scaled by a factor of $(1/M^2)$ where M represents the magnification of the microendoscope (2.8X). Images were collected at a resolution of 1024×1024 (pixel size of ~0.16 microns) and a z step size of ~0.51 microns in the sample plane. Due to our high sampling rate, we reduced the noise by using MATLAB to downsample the images using 2×2 binning. In the z plane, two consecutive images were averaged together to reduce the number of individual images in the z-stack. The resulting images had a resolution of 512×512 (pixel size of ~0.32 microns) and a z step size of 1.02 microns. Fiji was used to extract the mean lateral and axial intensity profiles of the beads which were fit to a gaussian curve to solve for the full width half maximum (FWHM). The FWHM of five, 0.2-micron beads in the lateral and axial directions were ~0.86 microns and ~9.6 microns respectively.
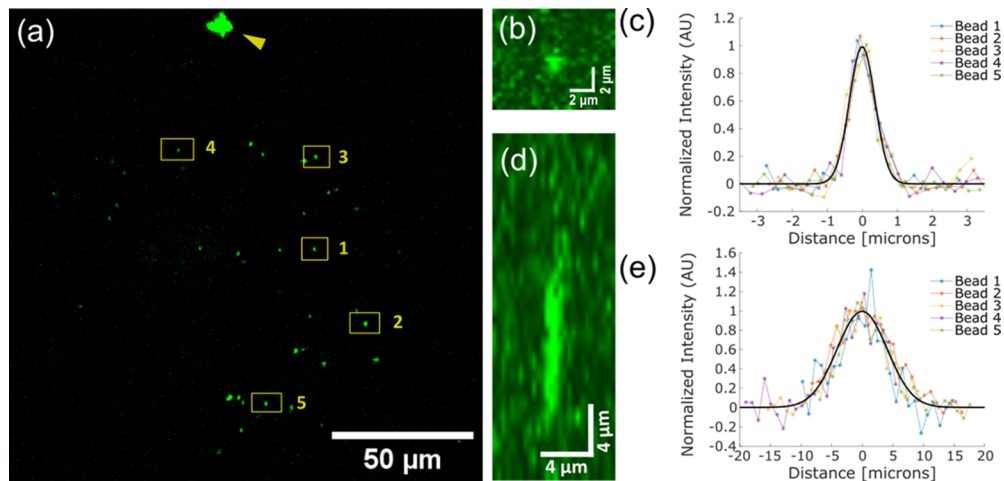

Fig. 9. Resolution analysis using 0.2-micron beads suspended in agarose. (a) Maximum intensity projection of green, fluorescent beads over the GRIN microendoscope FOV. The yellow arrow represents a 2.0-micron diameter bead in the sample. Beads selected for FWHM analysis are marked by numbers 1 through 5. (b) Single image plane of Bead 3 in the lateral (XY) plane. (c) Normalized fluorescent intensity of all 5 beads in the XY plane. The black line represents a gaussian curve with a FWHM of ~0.86 microns. (d) Single plane orthogonal view of Bead 3 in the axial (XZ) plane. (e) Normalized fluorescent intensity of all 5 beads in the Z plane. The black line represents a gaussian curve with a FWHM of ~9.6 microns.

3.2.4.   Transmission efficiency

The NA of the Olympus 10x objective (NA = 0.4) was much larger than the theoretical object space NA of the GRIN microendoscope (NA ~ 0.15). This means that substantially more light exited the 10x objective than entered the microendoscope. Therefore, an iris (SM1D25, THORLabs) was placed at the back aperture of the objective, and the diameter was stopped down until the beam in the sample plane of the microendoscope was visibly perturbed. The transmission efficiency of the microendoscope was calculated using the ratio of the power in
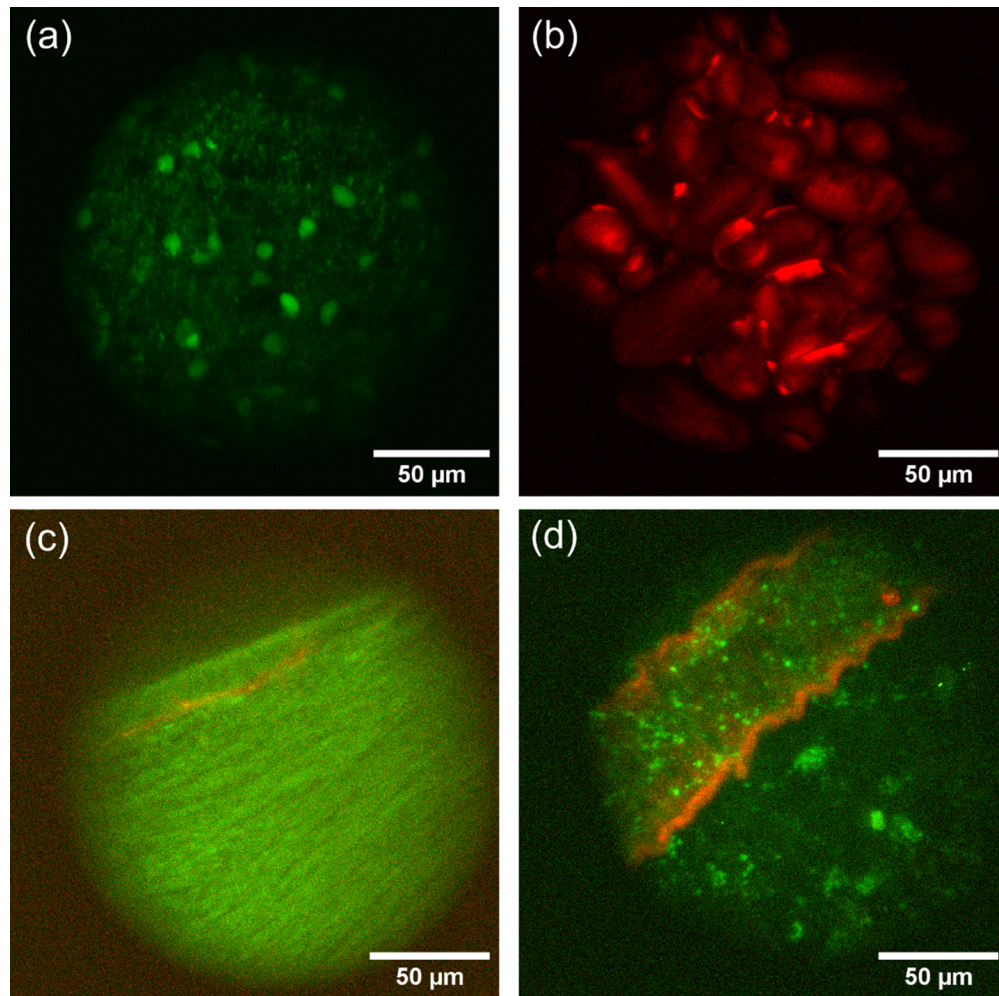
Fig. 10. Two-photon imaging through the GRIN microendoscope. (a) Image of EGFP labeled oligodendrocytes in the neocortex region of fixed mouse brain tissue (PLP-EGFP mouse), (b) SHG signal from potato starch granules, (c) Tissue autofluorescence (Green, 500–590 nm) and SHG (Red, 440-460 nm) from a blood vessel in fixed mouse brain tissue (C57BL/6 mouse), (d) Tissue autofluorescence and SHG from an unfixed human brain tissue sample from the temporal lobe.

the sample plane of the microendoscope to the power leaving the attenuated objective. The transmission efficiency of the GRIN microendoscope was 61% ± 7.9% (n = 3).

3.3. Proof-of-concept tissue imaging

The GRIN microendoscope was used to image EGFP labeled oligodendrocytes to verify that the prototype could visualize bright, cellular level signals in fixed mouse brain tissue (Fig. 10(a)). Oligodendrocyte images were captured using an average power of ~20 mW in the sample plane and without the aid of the pulse compressor. All the other images were collected with the pulse compressor in the beam path and circularly polarized light. We imaged potato starch granules to verify that the prototype could generate and collect SHG signal [42]. Images of potato starch granules were captured using an average power of ~11 mW in the sample plane (Fig. 10(b)).

Slices of fixed, C57BL/6 brain tissue were imaged for autofluorescence and SHG using an average power of ~19 mW in the sample plane (Fig. 10(c)). Because tissue processing and fixation procedures can exogenously affect autofluorescence, it was important to test our device with un-fixed tissue to verify that we could collect the signals of interest in a potential clinical situation [43–45]. Therefore, we imaged unfixed, human brain tissue that was recently resected from the temporal lobe of an epilepsy patient and suspended in a saline bath. This tissue was imaged for autofluorescence and SHG using an average power of ~40 mW in the sample plane (Fig. 10(d)). The proof-of-concept imaging presented in Fig. 10 demonstrates that the GRIN microendoscope is capable of two-photon imaging of EGFP, autofluorescence, and SHG in fixed, *ex-vivo* mouse brain tissue and autofluorescence and SHG from unfixed, *ex-vivo* human brain tissue.

4.　Conclusion

In this study, we performed label-free imaging to show that the human STN is distinguishable from the surrounding tissue using two-photon microscopy due to a distinct accumulation of autofluorescence. Preliminary immunohistochemical evidence suggests that the observed autofluorescence might be due to a build-up of lipofuscin in neurons and glia in this region (See Supplement 1, Fig S2). Lipofuscin is a protein and lipid based pigment that progressively accumulates in the lysosomes of post-mitotic cells during aging [46]. There are no immunohistochemical labels for lipofuscin, so it is typically identified by the broadband emission properties of its intrinsic autofluorescence [47]. We identified lipofuscin from its characteristically broad emission spectra (Fig. 6(c)) and the resistance to photobleaching.

In addition to imaging fluorescence, two-photon microscopy allows us to take advantage of other nonlinear imaging techniques like SHG. In SHG, two photons are upconverted to a single photon that has half the wavelength and twice the energy of the excitation light [48]. Two-photon imaging allows autofluorescence and SHG signals to be acquired simultaneously, and the resulting emissions from these two processes can be differentiated using dichroic mirrors and spectral filters [48]. In biological tissues, fibrillar collagen is an excellent source of SHG [49]. This allows for label-free imaging of blood vessels which has been previously demonstrated in conjunction with GRIN endomicroscopy [22–25].

To date, several long, rigid GRIN endoscopes have been engineered and used to image endogenous contrast in unlabeled tissues using two-photon microscopy, SHG, Optical Coherence Tomography (OCT), and coherent anti-Stokes Raman scattering (CARS) [22,24,25,28]. In 2012, Huland et al. developed a 8 cm long, 1 mm diameter GRIN endoscope with a ~200 micron FOV and a lateral and axial resolution of 0.85 microns and 7.4 microns respectively [22]. In 2018, Zirak et al. reported on an 18.7 cm long, 2.2 mm diameter GRIN endoscope with an 0.5 NA, achromatic objective; this device had a FOV of ~250 microns and a lateral resolution of 0.75 microns [25]. It is currently available as a commercial product through GRINTECH (GT-MO-050-009-ACR795/1029-10-50). In order to access the STN in an operating room setting, there is a need for an endoscope that is longer than 9 cm and compatible with a stereotactic cannula that has an inner diameter of ~1.1 mm. This endoscope will act as an image relay between a two-photon microscope and deep brain regions. We developed a microendoscope composed of four GRIN lenses that are separated by small annular, polyamide spacers. The lenses are 1 mm in diameter and are housed inside a polyamide tube with an outer diameter of 1.2 mm. The final prototype is approximately 18.6 cm long.

The optical performance of the GRIN microendoscope was evaluated by placing our device into the beam path of a custom-built, two-photon microscope. The magnification of the GRIN microendoscope is ~2.8X and the FOV is between ~177-185 microns as the sample WD increases from 0 microns to 250 microns. Our microendoscope is capable of imaging 0.2-micron beads suspended in agarose with lateral and axial FWHMs of ~0.86 microns and ~9.6 microns respectively. From ZEMAX modeling, the theoretical imaging NA of the microendoscope

is 0.384. This corresponds to an illumination point spread function with lateral and axial diffraction limited $1/e$ radii of 0.53 and 5.8 microns respectively [50]. If we multiply these radii by $2*sqrt(ln(2))$, we can calculate the expected FWHM which is 0.88 microns in the lateral direction and 9.7 microns in the axial direction [50]. This is comparable with our experimental results.

The GRIN microendoscope could generate and collect endogenous, cellular level fluorescence and SHG signals from unlabeled biological samples. Imaging endogenous fluorophores typically requires higher laser intensities than extrinsically added fluorophores due to their relatively sparse distribution and smaller two-photon absorption cross-sections [51]. We were able to capture images of autofluorescence and SHG in fixed, mouse (C57BL/6) brain tissue and in resected, human temporal lobe tissue when using a pulse-compressor to correct for the effect of second-order dispersion in our system. In the future, additional testing will be conducted on both fixed and unfixed human STN tissue to validate that the GRIN microendoscope can identify this region from the surrounding tissues using autofluorescence. While SHG imaging is not critical for locating the STN, real-time imaging of blood vessels along the surgical trajectory may help reduce the risk of intracranial hemorrhage.

One of the limitations of this study is sample size, particularly regarding the imaging of human tissue. Many of these experiments were performed in a "proof-of-concept" capacity and will require additional testing to verify that the STN is reliably distinguishable from the surrounding tissue. Since the accumulation of lipofuscin is commonly associated with aging, it would be prudent to perform additional label-free, two-photon imaging of human brain tissue from donors who fall into the age range of the DBS target population (on average ~64 years old). Furthermore, additional analysis is needed to determine if the level of autofluorescence in the STN and surrounding tissue differs between controls and PD samples. This additional sampling could be used to further train and test our image classifiers and aid in the development of an automated method to localize the STN using two-photon microscopy.

The optical performance of our GRIN microendoscope is comparable with that of Huland et al. even though it is almost twice as long although the FOV is slightly smaller. GRIN lenses are notorious for optical aberrations; therefore, we might be able to improve the FOV and the resolution of the system by adding adaptive optics such as a deformable mirror or phase plate to correct for these aberrations. Reducing the magnification of the microendoscope could also potentially increase the observable FOV. Additionally, eliminating the internal air spaces between the GRIN lenses may improve the manufacturability and transmission efficiency of the microendoscope. Future improvements also include reducing the outer diameter of the microendoscope sheath to under 1.1 mm.

Ultimately, the goal is to design a two-photon endoscopic system that can be used in the operating room. This will require the whole system to be portable, unobtrusive, and user-friendly. The work presented in this paper represents the prototyping of a single component of this system: a GRIN microendoscope that acts as an image relay through a stereotactic cannula. This relay will be attached to a miniaturized, fiber-coupled microscope that the surgeon can manipulate by hand. This microscope will contain miniaturized versions of the scanning and collection optics found in a regular microscope such as microelectromechanical systems (MEMS) and/or electrowetting lenses, dichroic mirrors, filters, and PMTs [52–54]. A fiber laser can be used as the two-photon excitation source and is a good way to reduce the size and complexity of the microscope's overall optical path. Finally, the microendoscope system needs to be integrated with a software interface that makes the imaging and interpretation of multiphoton signals intuitive for operating room personnel.

Multiphoton microscopy is an incredibly useful technique that is being increasingly utilized in both research and clinical applications. The novel GRIN microendoscope presented in this paper is a step towards label-free, *in-vivo* two-photon imaging of deep brain regions in humans.

Disclosures. The authors declare that there are no conflicts of interest related to this article.

Data availability. Data underlying the results presented in this paper are available from the authors upon reasonable request.

Supplemental document. See Supplement 1 for supporting content.

References

1. C. Marras, J. C. Beck, J. H. Bower, E. Roberts, B. Ritz, G. W. Ross, R. D. Abbott, R. Savica, S. K. Van Den Eeden, A. W. Willis, and C. M. Tanner, and P. G. on behalf of the Parkinson's Foundation, "Prevalence of Parkinson's disease across North America," npj Parkinson's Dis. **4**(1), 21 (2018).
2. J. Jankovic, "Parkinson's disease: clinical features and diagnosis," J. Neurol., Neurosurg. Psychiatry **79**(4), 368–376 (2008).
3. W. Oertel and J. B. Schulz, "Current and experimental treatments of Parkinson disease: A guide for neuroscientists," J. Neurochem. **139**(Suppl 1), 325–337 (2016).
4. A. Abosch, L. Timmermann, S. Bartley, H. G. Rietkerk, D. Whiting, P. J. Connolly, D. Lanctin, and M. I. Hariz, "An International Survey of Deep Brain Stimulation Procedural Steps," Stereotact. Funct. Neurosurg. **91**(1), 1–11 (2013).
5. K. V. Slavin, K. R. Thulborn, C. Wess, and H. Nersesyan, "Direct Visualization of the Human Subthalamic Nucleus with 3 T MR Imaging," American Journal of Neuroradiology **27**(1), 80–84 (2006).
6. Y. Miyagi, F. Shima, and T. Sasaki, "Brain shift: an error factor during implantation of deep brain stimulation electrodes," J. Neurosurg. **107**(5), 989–997 (2007).
7. C. J. Hartmann, S. Fliegen, S. J. Groiss, L. Wojtecki, and A. Schnitzler, "An update on best practice of deep brain stimulation in Parkinson's disease," Ther. Adv. Neurol. Disord. **12**, 175628641983809 (2019).
8. J. D. Rolston, D. J. Englot, P. A. Starr, and P. S. Larson, "An unexpectedly high rate of revisions and removals in deep brain stimulation surgery: Analysis of multiple databases," Parkinsonism Relat. Disord. **33**, 72–77 (2016).
9. Z. Cui, L. Pan, H. Song, X. Xu, B. Xu, X. Yu, and Z. Ling, "Intraoperative MRI for optimizing electrode placement for deep brain stimulation of the subthalamic nucleus in Parkinson disease," J. Neurosurg. **124**(1), 62–69 (2016).
10. J. B. Kim, M. Shirley, L. Albert, and M. R. Ahmed, "Accuracy of deep brain stimulation electrode placement using intraoperative computed tomography without microelectrode recording," J. Neurosurg. **119**(2), 301–306 (2013).
11. T. Foltynie, L. Zrinzo, I. Martinez-Torres, E. Tripoliti, E. Petersen, E. Holl, I. Aviles-Olmos, M. Jahanshahi, M. Hariz, and P. Limousin, "MRI-guided STN DBS in Parkinson's disease without microelectrode recording: efficacy and safety," J. Neurol., Neurosurg. Psychiatry **82**(4), 358–363 (2011).
12. R. B. Kochanski and S. Sani, "Awake versus asleep deep brain stimulation surgery: technical considerations and critical review of the literature," Brain Sci. **8**(1), 17 (2018).
13. S. K. Akshulakov, T. T. Kerimbayev, M. Y. Biryuchkov, Y. A. Urunbayev, D. S. Farhadi, and V. A. Byvaltsev, "Current trends for improving safety of stereotactic brain biopsies: advanced optical methods for vessel avoidance and tumor detection," Front. Oncol. **9**, 947 (2019).
14. H. Mehidine, M. Sibai, F. Poulon, J. Pallud, P. Varlet, M. Zanello, B. Devaux, and D. Abi Haidar, "Multimodal imaging to explore endogenous fluorescence of fresh and fixed human healthy and tumor brain tissues," J. Biophotonics **12**, e201800178 (2019).
15. H. Ramakonar, B. C. Quirk, R. W. Kirk, J. Li, A. Jacques, C. R. P. Lind, and R. A. McLaughlin, "Intraoperative detection of blood vessels with an imaging needle during neurosurgery in humans," Sci. Adv. **4**(12), eaav4992 (2018).
16. W. Liang, G. Hall, B. Messerschmidt, M.-J. Li, and X. Li, "Nonlinear optical endomicroscopy for label-free functional histology in vivo," Light: Sci. Appl. **6**(11), e17082 (2017).
17. A. Terman and U. T. Brunk, "Lipofuscin: mechanisms of formation and increase with age," APMIS **106**(1-6), 265–276 (1998).
18. W. M. Lee and S. H. Yun, "Adaptive aberration correction of GRIN lenses for confocal endomicroscopy," Opt. Lett. **36**(23), 4608–4610 (2011).
19. G. Meng, Y. Liang, S. Sarsfield, W.-c. Jiang, R. Lu, J. T. Dudman, Y. Aponte, and N. Ji, "High-throughput synapse-resolving two-photon fluorescence microendoscopy for deep-brain volumetric imaging in vivo," eLife **8**, e40805 (2019).
20. F. Helmchen, W. Denk, and J. N. Kerr, "Miniaturization of two-photon microscopy for imaging in freely moving animals," Cold Spring Harbor protocols **2013**(10), 904–913 (2013).
21. J. C. Jung, A. D. Mehta, E. Aksay, R. Stepnoski, and M. J. Schnitzer, "In vivo mammalian brain imaging using one- and two-photon fluorescence microendoscopy," J. Neurophysiol. **92**(5), 3121–3133 (2004).

22. D. M. Huland, C. M. Brown, S. S. Howard, D. G. Ouzounov, I. Pavlova, K. Wang, D. R. Rivera, W. W. Webb, and C. Xu, "In vivo imaging of unstained tissues using long gradient index lens multiphoton endoscopic systems," Biomed. Opt. Express **3**(5), 1077–1085 (2012).

23. A. Wingert, H. Seim, S. Schürmann, R. H. A. Fink, and M. Vogel, "Signal efficiency in gradient index lens based two photon microscopy," Open Journal of Biophysics. **03**(01), 43–50 (2013).

24. D. M. Huland, M. Jain, D. G. Ouzounov, B. D. Robinson, D. S. Harya, M. M. Shevchuk, P. Singhal, C. Xu, and A. K. Tewari, "Multiphoton gradient index endoscopy for evaluation of diseased human prostatic tissue ex vivo," J. Biomed. Opt **19**(11), 116011 (2014).

25. P. Zirak, G. Matz, B. Messerschmidt, T. Meyer, M. Schmitt, J. Popp, O. Uckermann, R. Galli, M. Kirsch, M. J. Winterhalder, and A. Zumbusch, "Invited Article: A rigid coherent anti-Stokes Raman scattering endoscope with high resolution and a large field of view," APL Photonics **3**(9), 092409 (2018).

26. D. Septier, V. Mytskaniuk, R. Habert, D. Labat, K. Baudelle, A. Cassez, G. Brévalle-Wasilewski, M. Conforti, G. Bouwmans, H. Rigneault, and A. Kudlinski, "Label-free highly multimodal nonlinear endoscope," Opt. Express **30**(14), 25020–25033 (2022).

27. K. König, A. Ehlers, I. Riemann, S. Schenkl, R. Bückle, and M. Kaatz, "Clinical two-photon microendoscopy," Microsc. Res. Tech. **70**(5), 398–402 (2007).

28. H. Schulz-Hildebrandt, M. Pieper, C. Stehmar, M. Ahrens, C. Idel, B. Wollenberg, P. König, and G. Hüttmann, "Novel endoscope with increased depth of field for imaging human nasal tissue by microscopic optical coherence tomography," Biomed. Opt. Express **9**(2), 636–647 (2018).

29. J. T. Ting, B. Kalmbach, P. Chong, R. de Frates, C. D. Keene, R. P. Gwinn, C. Cobbs, A. L. Ko, J. G. Ojemann, R. G. Ellenbogen, C. Koch, and E. Lein, "A robust ex vivo experimental platform for molecular-genetic dissection of adult human neocortical cell types and circuits," Sci. Rep. **8**(1), 8407 (2018).

30. L. Mostaço-Guidolin, N. L. Rosin, and T.-L. Hackett, "Imaging collagen in scar tissue: developments in second harmonic generation microscopy for biomedical applications," Int. J. Mol. Sci. **18**(8), 1772 (2017).

31. J. Schindelin, I. Arganda-Carreras, E. Frise, V. Kaynig, M. Longair, T. Pietzsch, S. Preibisch, C. Rueden, S. Saalfeld, B. Schmid, J.-Y. Tinevez, D. J. White, V. Hartenstein, K. Eliceiri, P. Tomancak, and A. Cardona, "Fiji: an open-source platform for biological-image analysis," Nat. Methods **9**(7), 676–682 (2012).

32. B. S. Mallon, H. E. Shick, G. J. Kidd, and W. B. Macklin, "Proteolipid promoter activity distinguishes two populations of NG2-positive cells throughout neonatal cortical development," J. Neurosci. **22**(3), 876–885 (2002).

33. R. M. Haralick, K. Shanmugam, and I. Dinstein, "Textural features for image classification," IEEE Trans. Syst., Man, Cybern. **3**(6), 610–621 (1973).

34. L. Nanni, S. Brahnam, S. Ghidoni, E. Menegatti, and T. Barrier, "Different approaches for extracting information from the co-occurrence matrix," PLoS One **8**(12), e83554 (2013).

35. G. Castellano, L. Bonilha, L. M. Li, and F. Cendes, "Texture analysis of medical images," Clin. Radiol. **59**(12), 1061–1069 (2004).

36. A. Kassner and R. E. Thornhill, "Texture Analysis: A Review of Neurologic MR Imaging Applications," American Journal of Neuroradiology **31**(5), 809–816 (2010).

37. F. B. Legesse, A. Medyukhina, S. Heuke, and J. Popp, "Texture analysis and classification in coherent anti-Stokes Raman scattering (CARS) microscopy images for automated detection of skin cancer," Comput. Med. Imaging Graph. **43**, 36–43 (2015).

38. Z. Xiao, Y. Ding, T. Lan, C. Zhang, C. Luo, and Z. Qin, "Brain MR Image Classification for Alzheimer's Disease Diagnosis Based on Multifeature Fusion," Comput. Math. Methods Med. **2017**, 1952373 (2017).

39. D. R. Stirling, M. J. Swain-Bowden, A. M. Lucas, A. E. Carpenter, B. A. Cimini, and A. Goodman, "CellProfiler 4: improvements in speed, utility and usability," BMC Bioinformatics **22**(1), 433 (2021).

40. D. Curran-Everett, "Multiple comparisons: philosophies and illustrations," American Journal of Physiology-Regulatory, Integrative and Comparative Physiology **279**(1), R1–R8 (2000).

41. T. Lumley, P. Diehr, A. Scott Emerson, and L. Chen, "The Importance of the Normality Assumption in Large Public Health Data Sets," Annu. Rev. Public Health **23**(1), 151–169 (2002).

42. R. Carriles, D. N. Schafer, K. E. Sheetz, J. J. Field, R. Cisek, V. Barzda, A. W. Sylvester, and J. A. Squier, "Invited review article: Imaging techniques for harmonic and multiphoton absorption fluorescence microscopy," Rev. Sci. Instrum. **80**(8), 081101 (2009).

43. N. Sakr, O. Glazova, L. Shevkova, N. Onyanov, S. Kaziakhmedova, A. Shilova, M. V. Vorontsova, and P. Volchkov, "Characterizing and Quenching Autofluorescence in Fixed Mouse Adrenal Cortex Tissue," Int. J. Mol. Sci. **24**(4), 3432 (2023).

44. A. S. Davis, A. Richter, S. Becker, J. E. Moyer, A. Sandouk, J. Skinner, and J. K. Taubenberger, "Characterizing and Diminishing Autofluorescence in Formalin-fixed Paraffin-embedded Human Respiratory Tissue," J Histochem Cytochem. **62**(6), 405–423 (2014).

45. W. S. Pyon, D. T. Gray, and C. A. Barnes, "An Alternative to Dye-Based Approaches to Remove Background Autofluorescence From Primate Brain Tissue," Front. Neuroanat. **13**, 73 (2019).

46. K. L. Double, V. N. Dedov, H. Fedorow, E. Kettle, G. M. Halliday, B. Garner, and U. T. Brunk, "The comparative biology of neuromelanin and lipofuscin in the human brain," Cell. Mol. Life Sci. **65**(11), 1669–1682 (2008).

47. T. Jung, A. Höhn, and T. Grune, "Lipofuscin: Detection and Quantification by Microscopic Techniques," in *Advanced Protocols in Oxidative Stress II*, D. Armstrong, ed. (Humana Press, Totowa, NJ, 2010), pp. 173–193.

48. P. Campagnola, "Second harmonic generation imaging microscopy: applications to diseases diagnostics," Anal. Chem. **83**(9), 3224–3231 (2011).

49. X. Chen, O. Nadiarynkh, S. Plotnikov, and P. J. Campagnola, "Second harmonic generation microscopy for quantitative analysis of collagen fibrillar structure," Nat. Protoc. **7**(4), 654–669 (2012).

50. W. R. Zipfel, R. M. Williams, and W. W. Webb, "Nonlinear magic: multiphoton microscopy in the biosciences," Nat. Biotechnol. **21**(11), 1369–1377 (2003).

51. W. R. Zipfel, R. M. Williams, R. Christie, A. Y. Nikitin, B. T. Hyman, and W. W. Webb, "Live tissue intrinsic emission microscopy using multiphoton-excited native fluorescence and second harmonic generation," Proc. Natl. Acad. Sci. U.S.A. **100**(12), 7075–7080 (2003).

52. B. N. Ozbay, J. T. Losacco, R. Cormack, R. Weir, V. M. Bright, J. T. Gopinath, D. Restrepo, and E. A. Gibson, "Miniaturized fiber-coupled confocal fluorescence microscope with an electrowetting variable focus lens using no moving parts," Opt. Lett. **40**(11), 2553–2556 (2015).

53. X. Yu, L. Zhou, T. Qi, H. Zhao, and H. Xie, "MEMS enabled miniature two-photon microscopy for biomedical imaging," Micromachines **14**(2), 470 (2023).

54. K. Hwang, Y.-H. Seo, and K.-H. Jeong, "Microscanners for optical endomicroscopic applications," Micro and Nano Systems Letters **5**(1), 1 (2017).